

Electromagnetic enhancement of one-dimensional plasmonic hotspots along silver nanowire dimer examined by ultrafast surface enhanced fluorescence

Tamitake Itoh^{1*}, Yuko S. Yamamoto²

¹Health and Medical Research Institute, National Institute of Advanced Industrial
Science and Technology (AIST), Takamatsu, Kagawa 761-0395, Japan

²School of Materials Science, Japan Advanced Institute of Science and Technology
(JAIST), Nomi, Ishikawa 923-1292, Japan

*Corresponding author: tamitake-itou@aist.go.jp

Abstract

We investigated the spectral properties of electromagnetic (EM) enhancement of one-dimensional hotspots (1D HSs) generated between silver nanowire (NW) dimers. The EM enhancement spectra were directly derived by dividing the spectra of ultrafast surface-enhanced fluorescence (UFSEF) from single NW dimers with UFSEF obtained from large nanoparticle aggregates, which aggregate-by-aggregate variations in the UFSEF spectra were averaged out. Some NW dimers were found to exhibit EM enhancement spectra that deviated from the plasmon resonance Rayleigh scattering spectra, indicating that their EM enhancement was not generated by superradiant plasmons. These experimental results were examined by numerical calculation based on the EM mechanism by varying the morphology of the NW dimers. The calculations reproduced the spectral deviations as the NW diameter dependence of EM enhancement. Phase analysis of the enhanced EM near fields along the 1D HSs revealed that the dipole-quadrupole coupled plasmon, which is a subradiant mode, mainly generates EM enhancement for dimers with NW diameters larger than ~ 80 nm, which was consistent with scanning electron microscopic measurements.

I. Introduction

Effective cross-sections of optical responses for molecules inside the nanogaps or crevasses of nanoparticle (NP) aggregates are enhanced upon interaction with light tightly confined by plasmon resonance.¹ This phenomenon is called electromagnetic (EM) enhancement, which is expressed using the Purcell factor F , in addition to the radiative $\Delta\omega_R$ and nonradiative $\Delta\omega_{NR}$ decay rates of plasmon resonance as,¹

$$F_R = \frac{F\Delta\omega_R}{\Delta\omega_R + \Delta\omega_{NR}}. \quad (1)$$

Here, F is expressed as $F = \frac{Q(\lambda/n)^3}{4\pi^2V_P}$, where Q is the quality factor of the plasmon resonance, λ and n are the light wavelength and refractive index around the nanostructure, respectively, and V_P is the mode volume of the plasmon. Equation (1) indicates that an extremely small V_P in the nanogaps results in a large F_R . Particularly, spontaneous resonant Raman scattering comprising excitation and emission transitions undergoes twofold EM enhancement as $F_R(\lambda_{ex})F_R(\lambda_{em})$, where λ_{ex} and λ_{em} are the excitation and emission wavelengths, respectively.² The nanogaps inside NP aggregates reach a value of $<10^{10}$ for F_R ,^{2,3,4} enabling single molecule Raman spectroscopy.⁵⁻⁹ Such nanogaps are referred to as “hotspots” (HSs). HSs have been applied to various surface-enhanced spectroscopic methods such as surface-enhanced (resonant) Raman scattering (SE(R)RS), absorption (SEA), fluorescence (SEF), and their nonlinear

counterparts.¹ Furthermore, the EM coupling energy between plasmon resonance and molecular resonance at the HSs exceeds several hundred meVs,¹⁰⁻¹⁴ resulting in the generation of new physical and chemical processes, for example, molecular optomechanics¹⁵ and polariton chemistry.¹⁶ The values of V_P of HSs reach several tens of nm³,^{17,18} resulting in instability of enhanced optical signals.^{19,20} To resolve the problem while maintaining a large F_R , several HSs have been theoretically and experimentally developed.^{21,22} We have also developed one-dimensional HSs (1D HSs) where V_P is extended by several 10^4 times using the gaps or crevasses between silver nanowire (NW) dimers.^{23,24} In such development, the evaluation of the spectral properties of F_R is crucial for the clarification and optimization of these surface-enhanced spectroscopies and their related phenomena.²²

Rayleigh scattering cross-section σ_{sca} and extinction cross-section σ_{ext} spectroscopy have been used to evaluate the F_R of HSs.¹ In quantum optics, the interaction between a photon and a molecular exciton is expressed by the $\hat{\mathbf{A}} \cdot \hat{\mathbf{p}}$ and $\hat{\mathbf{A}}^2$ terms, where $\hat{\mathbf{A}}$ and $\hat{\mathbf{p}}$ are the operators of the vector potential and momentum, respectively.²⁵ The optical absorption (or emission) and Rayleigh scattering are expressed by the $\hat{\mathbf{A}} \cdot \hat{\mathbf{p}}$ and $\hat{\mathbf{A}}^2$ terms, respectively.²⁵ Fluorescence, Raman, and their nonlinear counterparts are described as two or more $\hat{\mathbf{A}} \cdot \hat{\mathbf{p}}$ terms.²⁶ Thus, the optical

absorption cross-section σ_{abs} spectroscopy of HSs should be used to evaluate F_R instead of σ_{sca} and σ_{ext} spectroscopies. Indeed, the spectral relationship between σ_{sca} (or σ_{ext}) and F_R becomes unclear with increasing size or degree of asymmetry of the aggregates, because subradiant plasmon resonance, which does not explicitly appear in σ_{sca} , becomes dominant to generate F_R .^{27,28} Thus, σ_{abs} spectroscopy was developed using the relationship $\sigma_{\text{abs}} = \sigma_{\text{ext}} - \sigma_{\text{sca}}$.^{29,30} However, this σ_{abs} spectroscopy is applicable only for small NP aggregates. In the case of large NP aggregates, almost all incident photons become extinct, resulting in the saturation of σ_{ext} and underestimation of σ_{abs} . Furthermore, σ_{abs} spectroscopy provides absorption of whole NP aggregates, including those outside HSs, resulting in the F_R of HSs becoming unclear in the σ_{abs} spectra.²⁹

In this study, we developed a spectroscopic technique to directly measure the F_R of HSs using the ultrafast surface-enhanced fluorescence (UFSEF) of dye molecules inside HSs. UFSEF appears as the spectral background of SERRS when the SEF rate is faster than the vibrational decay rate of the excited electronic states.^{31,32} We applied this spectroscopy to measure the F_R of the 1D HSs of the NW dimers, to which the σ_{abs} spectroscopy is not applicable. The F_R spectra were derived by dividing the spectra of UFSEF from the 1D HSs of single NW dimers by the UFSEF of large NP aggregate, where aggregate-by-aggregate spectral variations in F_R were averaged out. The derived

F_R spectra frequently exhibit blue shifts from the σ_{sca} spectra, suggesting that such F_R is not generated by superradiant plasmon but by subradiant plasmon. These results were examined using numerical calculation based on the EM mechanism by changing the NW diameter of the symmetric NW dimers and the degree of asymmetry of NW dimers. Calculations performed by changing the diameter reproduced the blueshifts in F_R well. The phase retardation of enhanced electric near-fields against incident fields was -180° , which indicates that the dipole-quadrupole coupled plasmon resonance,²⁷ which is subradiant, mainly generates F_R for dimers where the NW diameters are larger than 80 nm. These results are consistent with the scanning electron microscopic measurements.

II. Theoretical background

Here, we briefly explain the mechanism of UFSEF. The total radiative decay rate of a dye molecule in a free space is Γ_{r0} ($= \int \gamma_{r0}(\lambda_{\text{em}}) d\lambda_{\text{em}}$), where $\gamma_{r0}(\lambda_{\text{em}}) d\lambda_{\text{em}}$ is the radiative decay rate at λ_{em} .^{31,32} The total radiative decay rates of a molecule inside a HS enhanced by F_R are Γ_{Rad} ($= \int \gamma_{r0}(\lambda_{\text{em}}) F_R(\lambda_{\text{em}}) d\lambda_{\text{em}}$). The total internal relaxation rate of a molecule $\Gamma_{\text{int}} \sim 10^{12} \text{ s}^{-1}$ is generally significantly larger than $\Gamma_{r0} \sim 10^{8-9} \text{ s}^{-1}$ for fluorescent dye molecules.^{31,32} Thus, the fluorescent molecule emits a photon from the bottom of the vibrational state in the electronic excited state (S_1), as shown in Fig. 1(a1).³² Thus,

the fluorescence spectrum does not have excitation laser wavelength dependence, as shown in Fig. 1(a2). However, $F_R \sim 10^5$ inside the HSs yields $F_{\text{int}} (10^{12} \text{ s}^{-1}) < \Gamma_{\text{Rad}} (10^5 \times 10^9 \text{ s}^{-1})$, indicating that SEF has a component of photons emitted from the vibrational excited state in S_1 before relaxing to the bottom of S_1 , as shown in Fig. 1(b1).³² Such emission is called UFSEF, and appears as the background of the SERRS spectrum. The UFSEF spectra exhibit blue shifts in the highest energy from conventional fluorescence and becomes dependent on the excitation laser wavelength as shown in Fig. 1(b2).³²

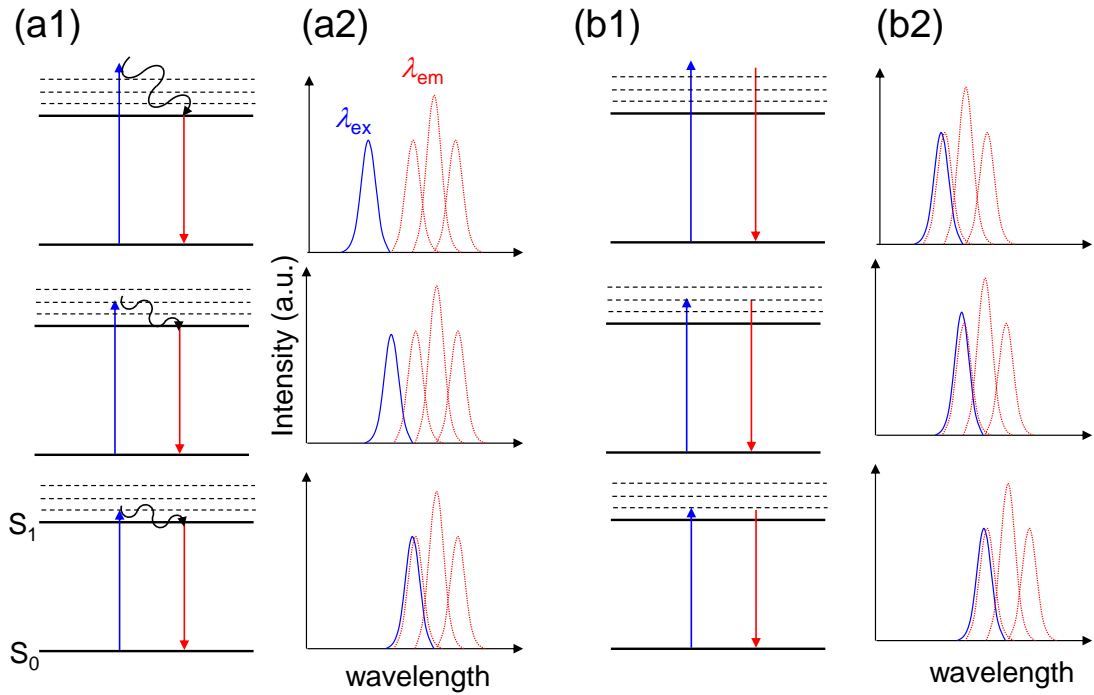


FIG. 1. (a1) Energy-level diagrams for excitation transition by laser light (blue arrows) and conventional SEF transition ($F_{\text{int}} \gg \Gamma_{\text{Rad}}$) (red arrows). (a2) Envelopes of a blue

and three red curves correspond to excitation and fluorescent spectra, respectively. Vibrational relaxations are indicated by wavy arrows. (b1) Energy-level diagrams for excitation transition by laser light (blue arrows) and UFSEF transition ($\Gamma_{\text{int}} < \Gamma_{\text{Rad}}$) (red arrows). (b2) Envelopes of a blue and three red curves correspond to UFSEF spectra. S_0 and S_1 indicate the ground and lowest excited electronic states. Dashed lines indicate vibrational excited states.

The relationships between the $\hat{\mathbf{A}} \cdot \hat{\mathbf{p}}$ and $\hat{\mathbf{A}}^2$ terms and molecular optical processes (i.e., absorption, Rayleigh scattering, fluorescence, and Raman scattering) are explained to show the importance of the $\hat{\mathbf{A}} \cdot \hat{\mathbf{p}}$ term for fluorescence and Raman or UFSEF and SE(R)RS.²⁶ Here, \hat{H}_{int} , which indicates the Hamiltonian for EM interactions between the electrons and the EM field, is described as follows:

$$\hat{H}_{\text{int}} = \sum_{i=1}^N -\frac{e_i}{m_i} \hat{\mathbf{A}}(\mathbf{r}_i) \cdot \hat{\mathbf{p}}_i + \sum_{i=1}^N \frac{e_i^2}{2m_i} \hat{\mathbf{A}}^2(\mathbf{r}_i), \quad (2)$$

where e_i , m_i , and \mathbf{r}_i are the charge, effective mass, and position of the i -th electron, respectively.²⁵ The first and second terms on the right side of Eq. (2) are called the $\hat{\mathbf{A}} \cdot \hat{\mathbf{p}}$ term ($\hat{H}_{\text{int}}(AP)$) and $\hat{\mathbf{A}}^2$ term ($\hat{H}_{\text{int}}(A^2)$), respectively. The time-independent Schrödinger equation for the stationary states of a system without EM interactions is

$$\left(\hat{H}_e + \hat{H}_{\text{ph}}\right)\Psi_0^n(\mathbf{r}) = E_0^n\Psi_0^n(\mathbf{r}), \quad n = 1, 2, 3, \dots, \quad (3)$$

where \hat{H}_e and \hat{H}_{ph} are Hamiltonians for the electrons and the EM field, respectively, and $\Psi_0^n(\mathbf{r})$ and E_0^n represent the wave function and energy of the system in the n -th state (superscript) for the unperturbed system (subscript 0), respectively.²⁵ Assuming that the system initially in Ψ_0^i at $t=0$ starts to be perturbed by \hat{H}_{int} , the probability $|b_f(t)|^2$ for the system finally to be Ψ_0^f can be derived using the first- and second-order perturbation terms as

$$|b_f(t)|^2 \propto \left| \langle \Psi_0^f | \hat{H}_{\text{int}} | \Psi_0^i \rangle + \sum_{n \neq i} \langle \Psi_0^f | \hat{H}_{\text{int}} | \Psi_0^n \rangle \langle \Psi_0^n | \hat{H}_{\text{int}} | \Psi_0^i \rangle \right|^2, \quad (4)$$

where $\langle \Psi_0^f | \hat{H}_{\text{int}} | \Psi_0^i \rangle$ and $\sum_{n \neq i} \langle \Psi_0^f | \hat{H}_{\text{int}} | \Psi_0^n \rangle \langle \Psi_0^n | \hat{H}_{\text{int}} | \Psi_0^i \rangle$ indicate the transitions related to the first- and second-order perturbation terms, respectively, and the subscripts f and n denote the final and intermediate states, respectively.²⁶

The matrix element $\langle \Psi_0^f | \hat{H}_{\text{int}} | \Psi_0^i \rangle$ in Eq. (4) can be separated into $\langle \Psi_0^f | \hat{H}_{\text{int}}(AP) | \Psi_0^i \rangle$ and $\langle \Psi_0^f | \hat{H}_{\text{int}}(A^2) | \Psi_0^i \rangle$ using Eq. (2). $\langle \Psi_0^f | \hat{H}_{\text{int}}(AP) | \Psi_0^i \rangle$ corresponds to one-photon absorption or one-photon emission. It is well-known as the Fermi's golden rule, and is given by

$$\langle \Psi_0^f | \hat{H}_{\text{int}}(AP) | \Psi_0^i \rangle \propto \sum_{i=1}^N \frac{\mathbf{i}}{\hbar} (\varepsilon_f - \varepsilon_i) \langle f | e_{i\mathbf{r}_i} | i \rangle, \quad (5)$$

where $|i\rangle$ and $|f\rangle$ are the eigenfunctions of the initial and final states of the electron

system, respectively, and ε_i and ε_f are their respective energies. $\langle f | e_{i\mathbf{r}_i} | i \rangle \neq 0$ can be nonzero for $|i\rangle \neq |f\rangle$.²⁶ The $\hat{\mathbf{A}}^2$ terms $\langle \Psi_0^f | \hat{H}_{\text{int}}(A^2) | \Psi_0^i \rangle$ can be described as

$$\langle \Psi_0^f | \hat{H}_{\text{int}}(A^2) | \Psi_0^i \rangle \propto \sum_{i=1}^N \frac{\mathbf{i}}{\hbar} \langle f || i \rangle. \quad (6)$$

Here, $\langle f || i \rangle$ can be nonzero for $|i\rangle = |f\rangle$, meaning that the two-photon process in Eq. (6) corresponds to Rayleigh scattering.²⁶

The transitions are evaluated using the second-order perturbation term $\sum_{n \neq i} \langle \Psi_0^f | \hat{H}_{\text{int}} | \Psi_0^n \rangle \langle \Psi_0^n | \hat{H}_{\text{int}} | \Psi_0^i \rangle$ in Eq. (4). The matrix elements corresponding to the Rayleigh and Raman scattering should include $\hat{H}_{\text{int}}(AP)$ as a nonzero term. Thus, this term can be rewritten as:

$$\sum_{n \neq i} \langle \Psi_0^f | \hat{H}_{\text{int}}(AP) | \Psi_0^n \rangle \langle \Psi_0^n | \hat{H}_{\text{int}}(AP) | \Psi_0^i \rangle. \quad (7)$$

The matrix elements in Eq. (7) mainly contribute to Raman scattering for $|i\rangle \neq |f\rangle$.²⁶

In summary, absorption (or emission) and Rayleigh scattering are generated by $\langle \Psi_0^f | \hat{H}_{\text{int}}(AP) | \Psi_0^i \rangle$ and $\langle \Psi_0^f | \hat{H}_{\text{int}}(A^2) | \Psi_0^i \rangle$, respectively, as shown in Figs. 2(a) and 2(b). Fluorescence involves a two-step process of two terms of $\langle \Psi_0^f | \hat{H}_{\text{int}}(AP) | \Psi_0^i \rangle$, as shown in Fig. 2(c). Raman scattering occurs via $\sum_{n \neq i} \langle \Psi_0^f | \hat{H}_{\text{int}}(AP) | \Psi_0^n \rangle \langle \Psi_0^n | \hat{H}_{\text{int}}(AP) | \Psi_0^i \rangle$, as shown in Fig. 2(d). Regarding the contribution of $\hat{H}_{\text{int}}(AP)$ to fluorescence and Raman scattering, the spectral shapes of F_R in Eq. (1) are correlated to UFSEF and SE(R)RS.

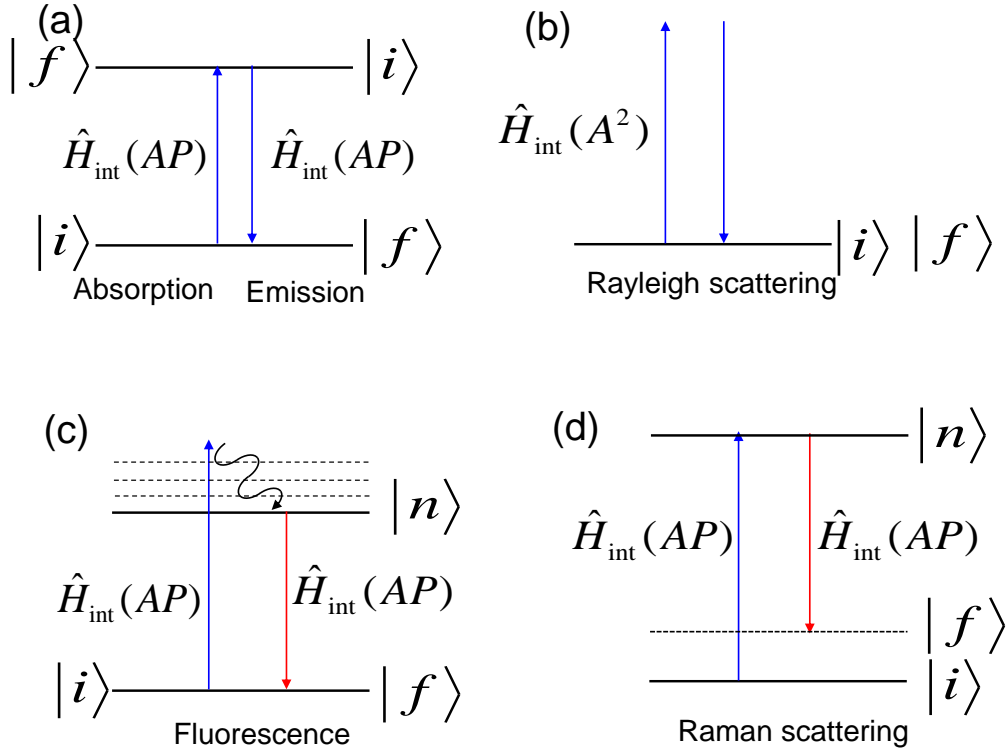


FIG. 2. (a) Energy-level diagrams of absorption and emission transitions from initial $|i\rangle$ to final state $|f\rangle$, respectively, triggered by $\hat{H}_{\text{int}}(AP)$. (b) Energy-level diagram of Rayleigh scattering transition from $|i\rangle$ to $|f\rangle$ ($|i\rangle = |f\rangle$) triggered by $\hat{H}_{\text{int}}(A^2)$. (c) Energy-level diagram of fluorescence process composed of absorption, vibrational relaxation (wavy arrow), and emission transitions from $|i\rangle$ to $|f\rangle$ via $|n\rangle$ by $\hat{H}_{\text{int}}(AP)$. Dashed lines indicate vibrational excited states. (d) Energy-level diagram of Raman process composed of absorption and emission transitions from $|i\rangle$ to $|f\rangle$ via $|n\rangle$ by $\hat{H}_{\text{int}}(AP)$. Dashed line indicates vibrational excited state $|f\rangle$.

III. Materials and experimental methods

The preparation methods of silver NW and NP samples are as described previously.^{33,34} The average NW diameter and length are approximately 60 nm and 10 μm , respectively. The NW suspension was dropped and dried on a glass plate with a rhodamine 6G (R6G) methanol solution ($\sim 5.0 \times 10^{-6}$ M). The effective concentration of the dye on the NWs was reduced by photobleaching most of the dye molecules adsorbed on the NW and glass surfaces via irradiation with a green laser beam. The reduction in concentration was confirmed by blinking and quenching of the UFSEF and fluorescence from both the NWs and glass surface, respectively.²³ The Rayleigh scattering spectra of the NW edges clearly exhibited oscillating structures due to the Fabry–Perot type resonance of the longitudinal surface plasmon mode, indicating that the NWs can be treated as single-crystalline rather than polycrystalline.²³

The dark-field images were measured by focusing the white light of a 50-W halogen lamp through a dark-field condenser (numerical aperture (NA) 0.92) to collect Rayleigh scattering light from single NW dimers. Superradiant plasmon resonance maxima of the NW dimers were observed in the Rayleigh scattering spectra. Figure 3(a) shows the measurement of a UFSEF image to obtain an entire 1D HS image. Unpolarized excitation laser beams with wavelengths 457, 473, 532, 561, and 633 nm were loosely focused using an objective lens (NA 0.2). The green closed circle in Fig.

3(b) indicates the focusing spot area ($\sim 200 \times 400 \mu\text{m}^2$) of the laser beam on a schematic of the 1D HS. A suitable laser wavelength was selected to evaluate the F_R spectra using UFSEF spectra. A $100\times$ objective lens, as shown in Fig. 3(a), was used to collect both Rayleigh scattering and UFSEF light from the NW dimer. Figures 3(c1) and 3(d1) show the dark-field images, and Figs. 3(c2)–3(c6) and 3(d2)–3(d6) show the UFSEF images of single NW dimer and a large NP aggregate at five excitation laser wavelengths, respectively. The Rayleigh scattering light and UFSEF light from an identical position are sent to a polychromator for spectroscopy through a pinhole to selectively measure the position at which the area is approximately $1.8 \times 1.8 \mu\text{m}^2$, as indicated in Fig. 3(b) by the dashed black circle.

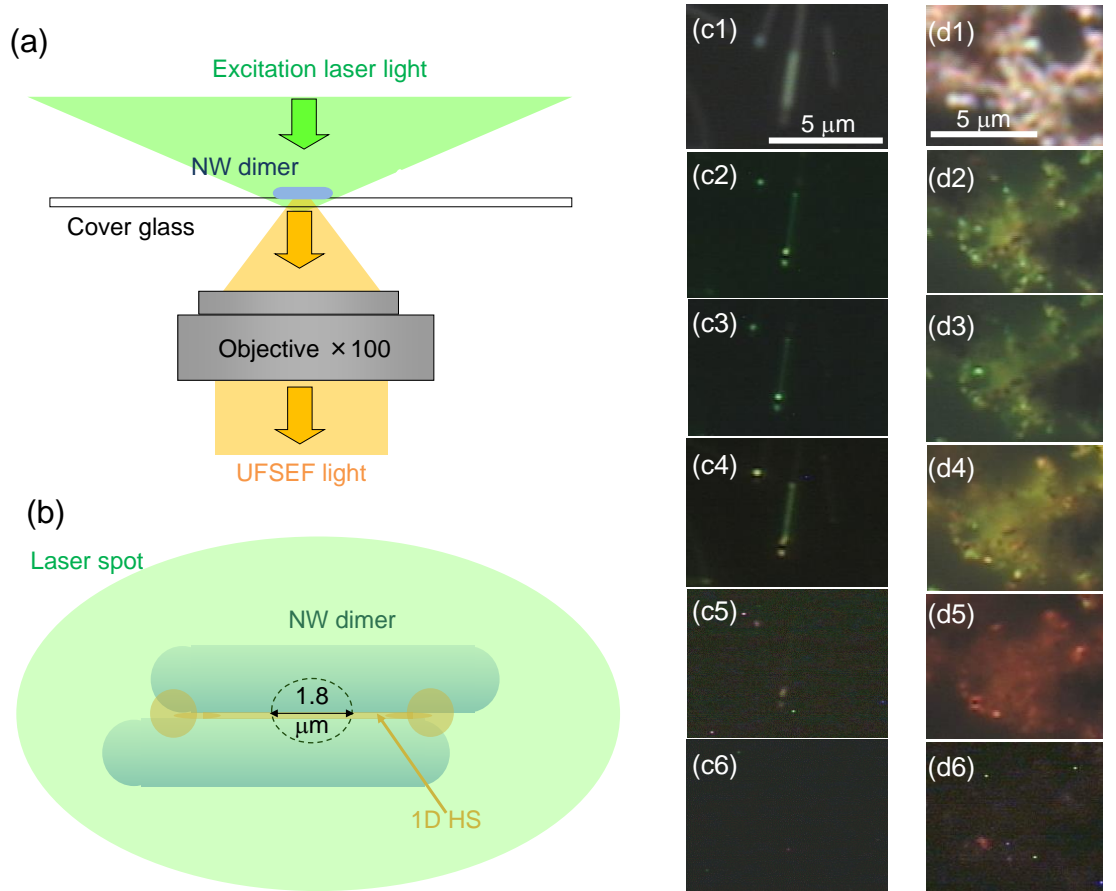


FIG. 3. (a) Experimental setup of laser beam excitation for NW dimer. NW dimers placed on the cover glass are excited from above and forward UFSEF light is detected. (b) Schematic of the UFSEF image of entire 1D HS illustrated with orange closed circles and a line. The large green spot indicates a focusing laser spot of excitation light. The dashed black open circle is detection area. (c1)–(c6) and (d1)–(d6) dark-field image (c1, d1), UFSEF images with the five excitation laser wavelengths 457 (c2, d2), 473 (c3, d3), 532 (c4, d4), 561 (c5, c5), 633 (c6, c6) nm, respectively of single NW dimer and large NP aggregates. Scale bars in (c1)–(c6) and (d1)–(d6) are 5.0 μm.

IV. Results and discussion

Figures 4(a)–4(c) show the scanning electron microscopy (SEM, JSM-6700F JEOL) image of the NWs on an ITO glass surface, dark-field image, and UFSEF image of an identical area. The blue green color of NW dimers in Fig. 4(b) indicates that the plasmons of two NWs are coupled and their coupled resonance redshifts to the visible region.²³ The UFSEF activity of NW dimers in Fig. 4(c) reveals that the coupled plasmon resonance generates F_R along 1D HSs.²³ The UFSEF light propagates through 1D HSs, indicating both localized and propagating plasmons are involved in F_R .²⁴ Figure 4(d) shows the distribution of NW diameters estimated by the SEM images. Almost all NW diameters were distributed in the range of 40–90 nm. Figure 4(e) shows the degree of asymmetry of the NW dimers. The NW diameter ratios were within 2.0. These ratios are consistent with the distribution of the NW diameters shown in Fig. 4(d).

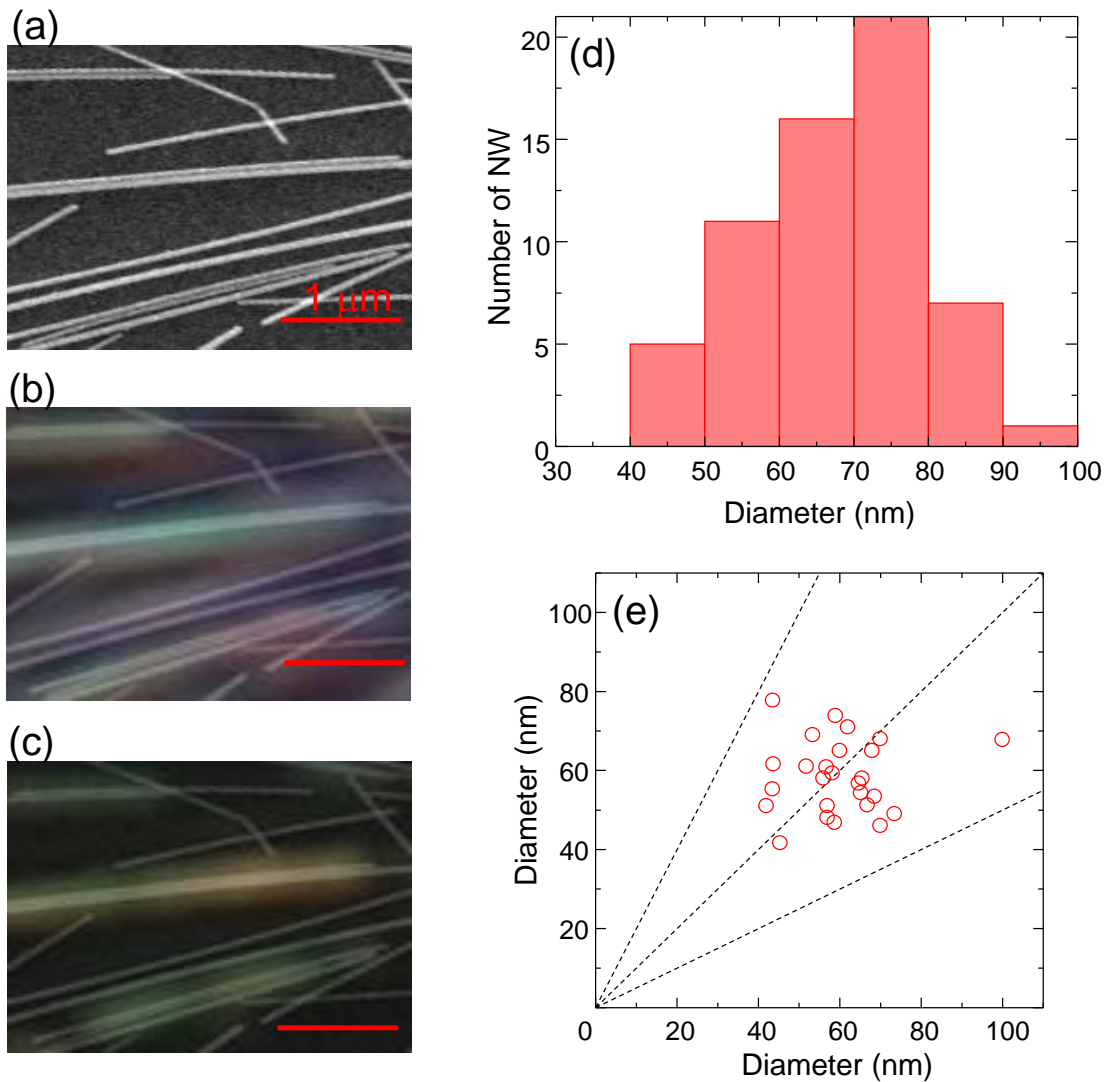


FIG. 4. (a) SEM image of NWs and NW dimers. (b) Superposition of the SEM and dark-field images. (c) Superposition of the SEM and UFSEF images. Scale bars in (a)–(c) are 1.0 μm . (d) Distribution of NW diameters estimated by SEM images. (e) Distribution of NW diameters of NW dimers estimated by SEM images. The three dashed lines indicate the diameter ratios between two NWs 0.5 (lower), 1.0 (middle), 2.0 (upper), respectively.

The UFSEF process comprises excitation and emission transitions, as shown in Fig. 2(c), expressed by two $\hat{\mathbf{A}} \cdot \hat{\mathbf{p}}$ terms.²⁶ Thus, the EM enhancement factor of the UFSEF is described as the product of the excitation enhancement factor $F_R(\lambda_{\text{ex}})$ and emission enhancement factor $F_R(\lambda_{\text{em}})$ using Eq. (1).¹ Thus, the cross-section of UFSEF $\sigma_{\text{UFSEF}}(\lambda_{\text{ex}}, \lambda_{\text{em}})$ is expressed as

$$\sigma_{\text{UFSEF}}(\lambda_{\text{ex}}, \lambda_{\text{em}}) = F_R(\lambda_{\text{ex}})F_R(\lambda_{\text{em}})\sigma_{\text{UFflo}}(\lambda_{\text{ex}}, \lambda_{\text{em}}), \quad (8)$$

where $\sigma_{\text{UFflo}}(\lambda_{\text{ex}}, \lambda_{\text{em}})$ is the cross-section of the ultrafast fluorescence without EM enhancement. Equation (8) indicates that the UFSEF spectrum is modulated by $F_R(\lambda_{\text{em}})$, which can originate from both superradiant and subradiant plasmon resonances. The purpose of this study was to experimentally extract F_R spectra from this spectral modulation. Extraction was performed by dividing the UFSEF spectra from the 1D HSs of single NW dimers (Figs. 3(c2)–3(c6)) by the UFSEF of large NP aggregate (Figs. 3(d2)–3(d6)). Such NP aggregate contain a large number of HSs which $F_R(\lambda_{\text{em}})$ values exhibit different spectral shapes. Thus, the $F_R(\lambda_{\text{em}})$ of the large NP aggregate is averaged, and becomes constant.^{19,32} Thus, its UFSEF spectrum can be expressed as

$$\propto F_R(\lambda_{\text{ex}})\sigma_{\text{UFflo}}(\lambda_{\text{ex}}, \lambda_{\text{em}}). \quad (9)$$

Thus, F_R spectrum of a single NW dimer can be experimentally derived by dividing Eq.

(8) by Eq. (9) as

$$F_R(\lambda_{em}) = \frac{F_R(\lambda_{ex})F_R(\lambda_{em})\sigma_{UFlo}(\lambda_{ex}, \lambda_{em})}{F_R(\lambda_{ex})\sigma_{UFlo}(\lambda_{ex}, \lambda_{em})}. \quad (10)$$

The UFSEF spectra of single-NW dimers were measured as per Eq. (8). Figure 5(a1) shows the σ_{sca} spectrum of a single NW dimer. The maximum of σ_{sca} at approximately 540 nm corresponds to the superradiant plasmon resonance. If the F_R for UFSEF is generated by subradiant plasmon resonance, the maximum of the F_R spectrum is not observed in the σ_{sca} spectrum, but is observed in the UFSEF spectrum. This is because the UFSEF spectrum is modulated by the F_R generated by both superradiant and subradiant resonances. Therefore, the UFSEF spectra of a single NW dimer were measured to determine the F_R maximum using multiple laser excitations. Figures 5(a2)–5(a6) show the λ_{ex} dependence of the UFSEF spectra for an identical NW dimer. The UFSEF spectral intensities were normalized to the excitation laser power. The normalized UFSEF intensity was the highest at λ_{ex} of 532 nm, which is close to the maximum of the absorption spectrum of the R6G $\propto \sigma_{UFlo}(\lambda_{ex})$, indicating the resonance effect of the R6G molecules. However, the entire structures of the UFSEF spectra are observed in Figs. 5(a2) and 5(a3), indicating that the spectral maximum of the F_R is located around these spectral regions.

The UFSEF spectra of large NP aggregates were measured as per Eq. (9).

Figure 5(b1) shows the σ_{sca} spectrum of the aggregate. The spectrum appears flat, indicating that the F_{R} spectra are averaged out and becomes also flat. Thus, one can obtain the UFSEF spectra corresponding to Eq. (9). Figures 5(b2)–5(b6) show the λ_{ex} dependence of the UFSEF spectra of the aggregate. The UFSEF spectral intensities were normalized to the excitation laser power. The normalized UFSEF intensity reaches the maximum at λ_{ex} 532 nm, which is also close to the absorption maximum of R6G, as shown in like Fig. 5(a4). It should be noted that the spectral properties in Figs. 5(b2)–5(b6) are different from those in Figs. 5(a2)–5(a6). For example, the UFSEF spectra in Figs. 5(b2) and 5(b3) appear significantly broader than those in Figs. 5(a2) and 5(a3). The UFSEF spectra in Figs. 5(a5) and 5(a6) show almost noise levels, but those in Figs. 5(b5) and 5(b6) clearly show the spectral structures. These different properties of the UFSEF spectra of the single NW dimer and large NP aggregate may be due to their F_{R} spectra.

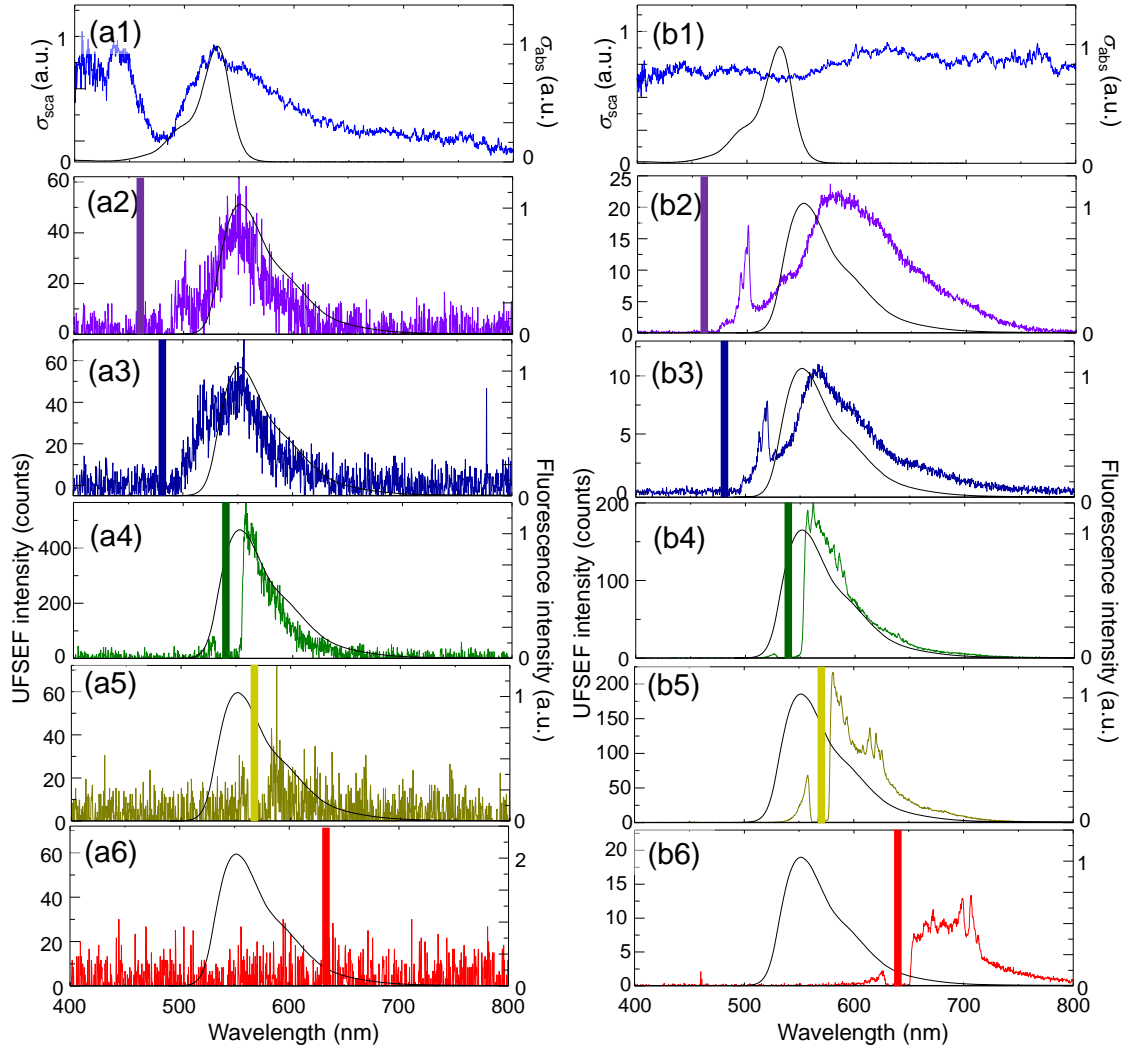


FIG. 5. (a1)–(a6) Spectra of σ_{sca} (a1) (blue curve), and UFSEF with the five excitation laser wavelengths 457 (a2) (purple curve), 473 (a3) (dark blue curve), 532 (a4) (green curve), 561 (a5) (dark yellow curve), 633 (a6) (red curve) nm, respectively, for single NW dimer. (b1)–(b6) Spectra of σ_{sca} (a1), and UFSEF with the five excitation laser wavelengths 457 (a2) (purple curve), 473 (a3) (dark blue curve), 532 (a4) (green curve), 561 (a5), 633 (a6) (red curve) nm, respectively, for a large NP aggregate. Black curves in (a1) and (b1) are absorption spectra of free R6G molecules. Black curves in (a2)–(a6)

and (b2)–(b6) are fluorescence spectra of free R6G molecules. Vertical lines curves in (a2)–(a6) and (b2)–(b6) indicate excitation laser wavelengths. Spike lines in (b2)–(b6) are SERRS spectra.

The procedure to experimentally obtain the F_R spectra are illustrated in Fig. 6, using Eq. (10). Figures 6(a) and 6(b) show the UFSEF spectra of a single NW dimer and a large NP aggregate, respectively. Figures 6(a) and 6(b) correspond to the UFSEF spectra in Eqs. (8) and (9), respectively. According to Eq. (10), the F_R spectrum in Fig. 6(c) was derived by dividing the UFSEF spectrum in Fig. 6(a) by that in Fig. 6(b). The contributions of superradiant and subradiant plasmon resonances to F_R are evaluated by comparing the derived F_R with the σ_{sca} spectra of a single NW dimer. The contribution of the subradiant resonance appears as a deviation between the F_R and σ_{sca} spectra. We define the maximum wavelengths of the σ_{sca} and F_R spectra as λ_{sca} and λ_F , respectively, as shown in Fig. 6(c).

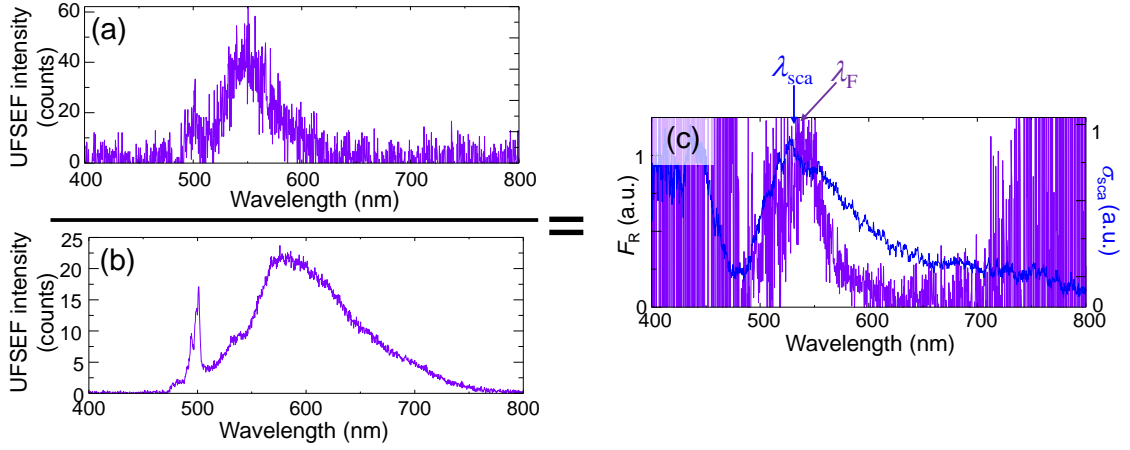


FIG. 6. Schematic for derivation of the F_R spectrum based on Eqs. (8)–(10). (a) and (b) Spectra of UFSEF of single NW dimer corresponding to Eq. (8) and a large NP aggregate corresponding to Eq. (9), respectively. (c) Spectra of F_R (purple curve) and σ_{sca} (blue curve). The position of the maxima of F_R and σ_{sca} at λ_F and λ_{sca} are indicated in the panel, respectively. The spectral regions in < 480 and > 700 nm were noise owing to weak signals of UFSEF and insertion of notch filter.

The F_R spectra were derived by dividing the UFSEF spectra of single NW dimers as shown in Figs. 5(a2)–5(a6) by the UFSEF spectra of the large NP aggregate as shown in Figs. 5(b2)–5(b6). Figures 7(a1)–7(a4) exhibit the obtained λ_{ex} dependence of the F_R spectra for a single NW dimer with σ_{sca} . With decreasing λ_{ex} , the entire envelope of F_R spectrum appeared in the spectral region where the UFSEF had sufficient intensity. The positions of λ_F appear near those of λ_{sca} in Figs. 7(a1) and 7(a2).

The results $\lambda_F \sim \lambda_{\text{sca}}$ indicate that F_R of this NW dimer was generated by superradiant plasmon resonance. However, the spectral slopes of F_R around 550–700 nm are much steeper than those of σ_{sca} . We examined the λ_{ex} dependence of F_R for several single NW dimers and found that the spectral maxima in F_R were always observed when $\lambda_{\text{ex}} = 457$ nm. Therefore, we measured the F_R spectra of several single-NW dimers using this λ_{ex} , as shown in Figs 7(b1)–7(b5). Figures 7(b1) and 7(b2) show that λ_F appears around λ_{sca} for NW dimers for which λ_{sca} is less than 550 nm. However, λ_F remained at approximately 550 nm even when λ_{sca} exceeded 550 nm, as shown in Figs. 7(b4) and 7(b5). This deviation between λ_F and λ_{sca} indicates the contribution of the subradiant plasmon resonance to F_R .

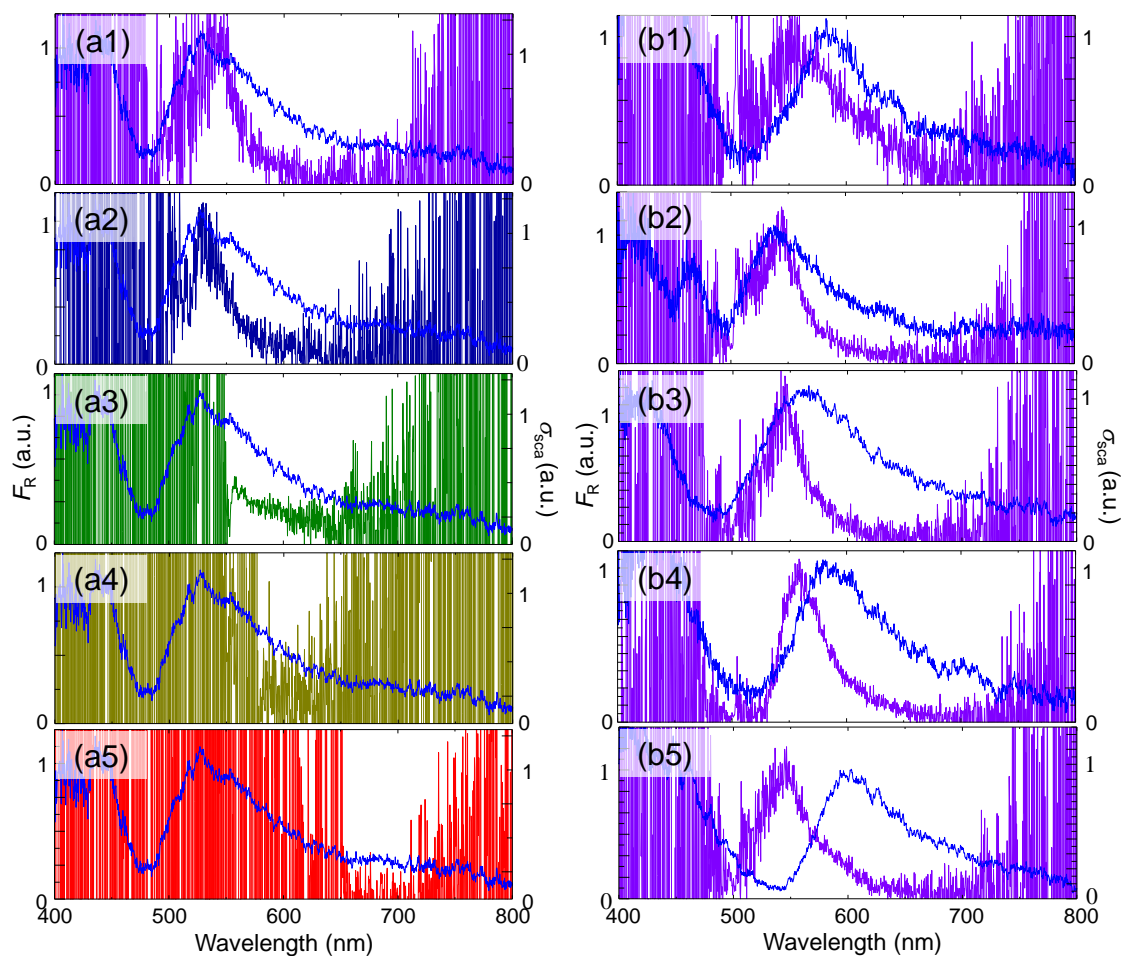


FIG. 7. (a1)–(a5) Spectra of σ_{sca} (blue curve) and F_{R} derived using UFSEF spectra of single NW dimer in FIG. 5. (a2)–(a6) and those of a large NP aggregate in FIG. 5. (b2)–(b6), respectively, based on Eq. (10) with the five excitation laser wavelengths 457 (a1) (purple curve), 473 (a2) (dark blue curve), 532 (a3) (green curve), 561 (a4) (dark yellow curve), 633 (a5) (red curve) nm, respectively. (b1)–(b5) Spectra of σ_{sca} (blue curve) and $F_{\text{R}}(\lambda_{\text{em}})$ (purple curves) derived using UFSEF of five single NW dimers and a large NP aggregate in FIG. 5. (b2) based on Eq. (10) with the excitation laser wavelength 457 nm.

The relationship between λ_F and λ_{sca} was investigated to confirm the contribution of superradiant and subradiant plasmon resonances to F_R . Figure 8 shows this relationship using 23 NW dimers with λ_{ex} of 457 nm. Two trends are observed, as indicated by the dashed lines. The first trend is that the λ_F values are almost the same as the λ_{sca} values for wavelengths below 550 nm. This trend indicates that superradiant plasmon resonance mainly generates F_R . The second trend is that the values of λ_F remain constant at approximately 550 nm, even with an increase in the values of λ_{sca} for wavelengths greater than 550 nm. This trend suggests the contribution of subradiant plasmon resonance to F_R .

The two trends observed in Fig. 8 indicate that the F_R spectra were generated by superradiant plasmon resonance for $\lambda_{sca} < 550$ nm and subradiant plasmon resonance for $\lambda_{sca} > 550$ nm. If this indication is correct, these two trends can be reproduced using EM calculations as a spectral correlation or as an uncorrelation between σ_{sca} and F_R . Thus, these trends were examined using the finite-difference time-domain (FDTD) method (EEM-FDM Version 5.1, EEM Co., Ltd., Japan). The complex refractive indices of the NWs were adopted from Ref. 35. The effective refractive index of the surrounding medium was set to 1.25 to ensure consistency between the calculated and

experimental σ_{sca} spectra of gold NPs.²⁶⁻²⁹ The experimentally obtained spectral relationships between σ_{sca} and F_R spectra were examined by changing the NW diameter of the symmetric NW dimers and by varying the degree of asymmetry of the NW dimers.

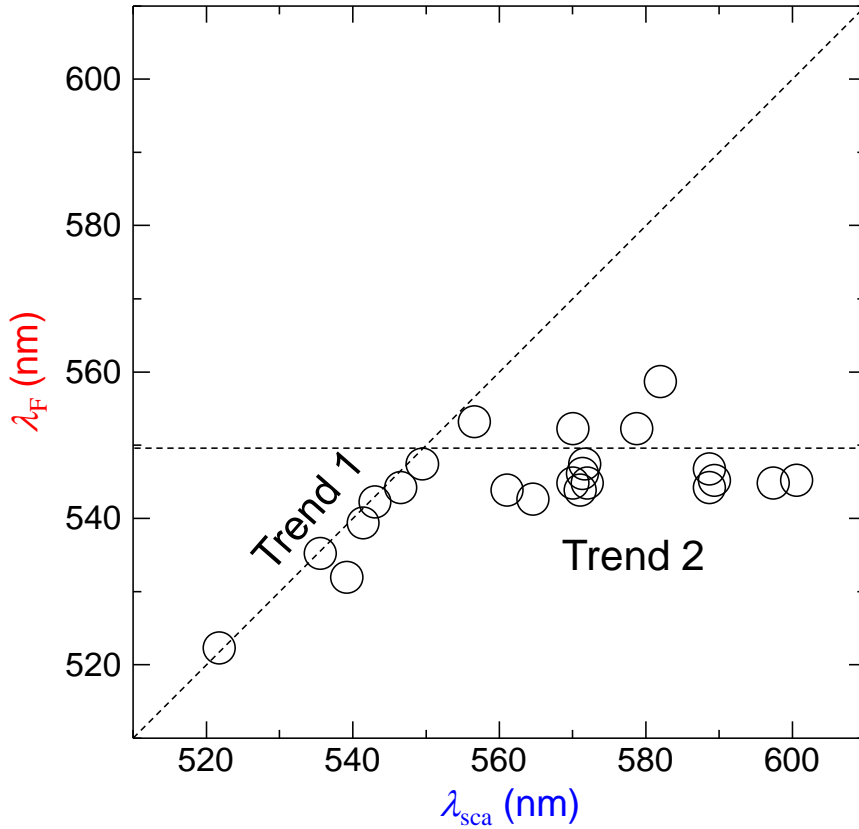


FIG. 8. Relationship between the λ_{sca} and λ_{F} for 23 single NW dimers exhibiting the two trends indicated by two black dashed lines.

Figures 9(a) and 9(b) show a setup of the FDTD calculation of a NW dimer with the coordinate system. The beam diameter for excitation light is infinite. The

excitation polarization direction was set perpendicular to the long axis of the NW dimer because an intense F_R of the 1D HS was generated along this direction by coupled plasmon resonance of both NWs.^{23,24} The NW dimer comprised two cylindrical NWs with hemispherical ends of diameters D_1 and D_2 . The gap distance was set to 0 nm, because the R6G molecules were added to NWs after their dimerization.²³ The lengths of the two NWs were 5.5 and 4.5 μm , respectively. Thus, the length of the 1D HS was 4.5 μm . The amplitude of the incident electric field $|E^I|$ is was set to be 1.0 V/m. Thus, the value of the calculated amplitude $|E^{\text{loc}}|$ was the same as the enhancement factor of electric field amplitude as $|E^{\text{loc}} / E^I|$. Note that the enhancement factor of electric field intensity $|E^{\text{loc}} / E^I|^2$ is equal to F_R as shown in Eq. (1). Figure 9(c) exhibits $|E^{\text{loc}}|$ along y-axis at $x, z = 0$ nm. The two peaks in the $|E^{\text{loc}}|$ distribution at $y = -9, 9$ nm are set to be the y position of 1D HS. Figure 9(d) shows $|E^{\text{loc}}|$ and the phase retardation θ_{PR} of E^{loc} against E^I along the z-axis at $x, y = 0, 9$ nm. The value of y is set to be the position of 1D HS as in Fig. 9(c). The oscillation patterns in $|E^{\text{loc}}|$ and θ_{PR} of E^{loc} are due to Fabry–Perot type interference.²³ Figure 9(e) shows the σ_{sca} spectrum and θ_{PR} of the NW dimer. The value of θ_{PR} is the averaged from -2.0 to 2.0 μm along the z-axis of 1D HS. Figure 9(f) shows the F_R spectrum and the θ_{PR} of the NW dimer. The value of F_R is also averaged from -2.0 to 2.0 μm along the z-axis of the 1D HS. The spectra of

σ_{sca} and F_{R} with the θ_{PR} were calculated along the 1D HSs for symmetric and asymmetric NW dimers to clarify the two trends observed in Fig. 8. First, these spectra of symmetric NW dimers are calculated by changing the diameter under the condition $D_1 = D_2$. Second, these spectra of asymmetric NW dimers are calculated by changing the ratios D_1/D_2 under the condition $D_1 = 60$ nm considering the distribution of NW diameters in Figs. 4(d) and 4(e). In these calculations, the nonlocal effect, which reduces F_{R} by Landau damping owing to unscreened surface electrons,³⁶ was not considered because Landau damping does not change the spectral shape of F_{R} , but rather its intensity.³⁷

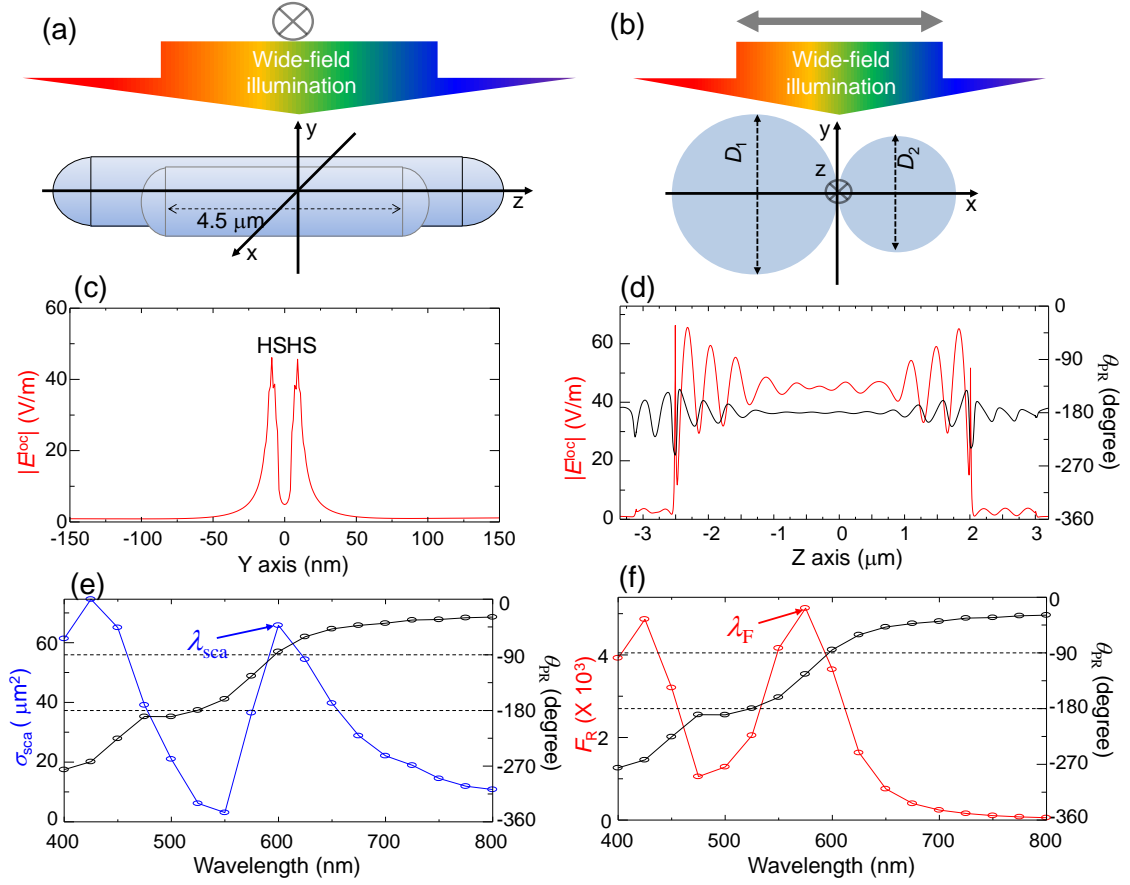


FIG. 9. (a) and (b) Image of an NW dimer with NW diameters D_1 and D_2 , respectively, with length of 1D HS of $4.5 \mu\text{m}$ and direction of the excitation light beam (rainbow arrow) with the coordinate system used for the FDTD calculations. The gray circle with cross and gray arrow in (a) and (b) indicate the direction of excitation light polarization, respectively. The gap distance was set to 0 nm . (c) Distribution of $|E^{\text{loc}}|$ (red curve) along the y-axis at $x, z = 0$ and 0 nm calculated with λ_{ex} of 525 nm . Two peaks, which are positions of HSHs, are located at $y = -9, 9 \text{ nm}$. (d) Distribution of $|E^{\text{loc}}|$ (red curve) with θ_{PR} (black curve) along the z axis at $x = 0$ and $y = 9 \text{ nm}$, calculated with λ_{ex} of 525 nm . (e) Calculated spectrum of σ_{sca} (blue curve) with θ_{PR} (upper and lower dashed lines

indicate -90° and -180° , respectively) of 1D HS for the NW dimer. (f) Calculated spectrum of F_R (red curve) with θ_{PR} (upper and lower dashed lines indicate -90° and -180° , respectively) of 1D HS for the NW dimer. The values of F_R and θ_{PR} are averaged from -2.0 to 2.0 μm along the z -axis of 1D HS for (e) and (f). Positions of λ_{sca} and λ_F are indicated in (e) and (f), respectively.

Figures 10(a1)–10(a3) show the spectra of σ_{sca} and F_R of the symmetric NW dimers obtained by changing D_1 from 30 to 100 nm under the condition $D_1 = D_2$ with respect to the NW diameter distribution in Fig. 4(d). As D_1 increases, the positions of λ_{sca} and λ_F deviate from each other, and finally, λ_F is located at the spectral dip of σ_{sca} . Figures 10(b1)–10(b3) show the spectra of σ_{sca} with θ_{PR} . The λ_{sca} redshifts with increasing D_1 , and is always located around the θ_{PR} of -90° , indicating that the maxima of σ_{sca} corresponds to the superradiant dipole-dipole (DD) coupled plasmon resonance of the two NWs.²⁷⁻²⁸ Figures 10(c1)–10(c3) show the spectra of F_R and θ_{PR} . The λ_F redshifts with increasing D_1 and is located at a θ_{PR} of approximately -90° until 60 nm, indicating that F_R is generated by DD-coupled plasmon resonance. However, the λ_F does not shift even upon increasing D_1 to greater than 60 nm, and is finally located at a θ_{PR} of approximately -180° . The value of -180° and the deviation between λ_{sca} and λ_F

indicate that F_R for $D_1 > 60$ nm is generated by a subradiant plasmon by receiving light energy from DD-coupled plasmon through near-field interaction.²⁶⁻²⁸ Furthermore, the same positions between λ_F and the spectral dip of σ_{sca} in Fig. 10(a3) also indicate that F_R is generated by subradiant plasmon resonance.^{26,27} Such subradiant resonance spectrally beside DD-coupled plasmon resonance has been attributed to dipole-quadrupole (DQ) coupled plasmon resonance.^{27,38} The charge distribution of DD- and DQ-coupled plasmon is illustrated in Fig. 10(d). The spectral broadening in dipole resonance by increasing in NW diameters results in the spectral overlapping between dipole and quadrupole resonances and arises DQ coupled resonance.^{27,38} Figure 10(e) shows the D_1 dependence of λ_{sca} and λ_F with θ_{PR} of -90° (DD-coupled plasmon resonance) and -180° (DQ-coupled plasmon resonance). The translucent red box indicates the range of the NW diameters: $40 \text{ nm} < D_1$ and $D_2 < 80 \text{ nm}$ by referring Fig. 4(d). Both λ_{sca} and λ_F follow the θ_{PR} of -90° for $D_1 < 60$ nm, indicating that the F_R is generated by DD-coupled plasmon resonance. With $D_1 > 60$ nm, the λ_{sca} keeps following θ_{PR} of -90° , but λ_F moves to θ_{PR} of -180° , indicating that DQ-coupled plasmon resonance becomes dominant in generating F_R for $D_1 > 60$ nm. Figure 10(f) shows the relationship between λ_{sca} and λ_F taking from Fig. 10(e) and the experimental relationship taking from Fig. 8. The translucent red box indicates the range of λ_{sca} for 40

$\sigma_m < D_1$ and $D_2 < 80$ nm. The two experimentally observed trends in Fig. 8 are clearly observed in the calculated relationship, indicating that the transition of the plasmon resonance generating F_R from DD- to DQ-coupled resonance causes these two trends.

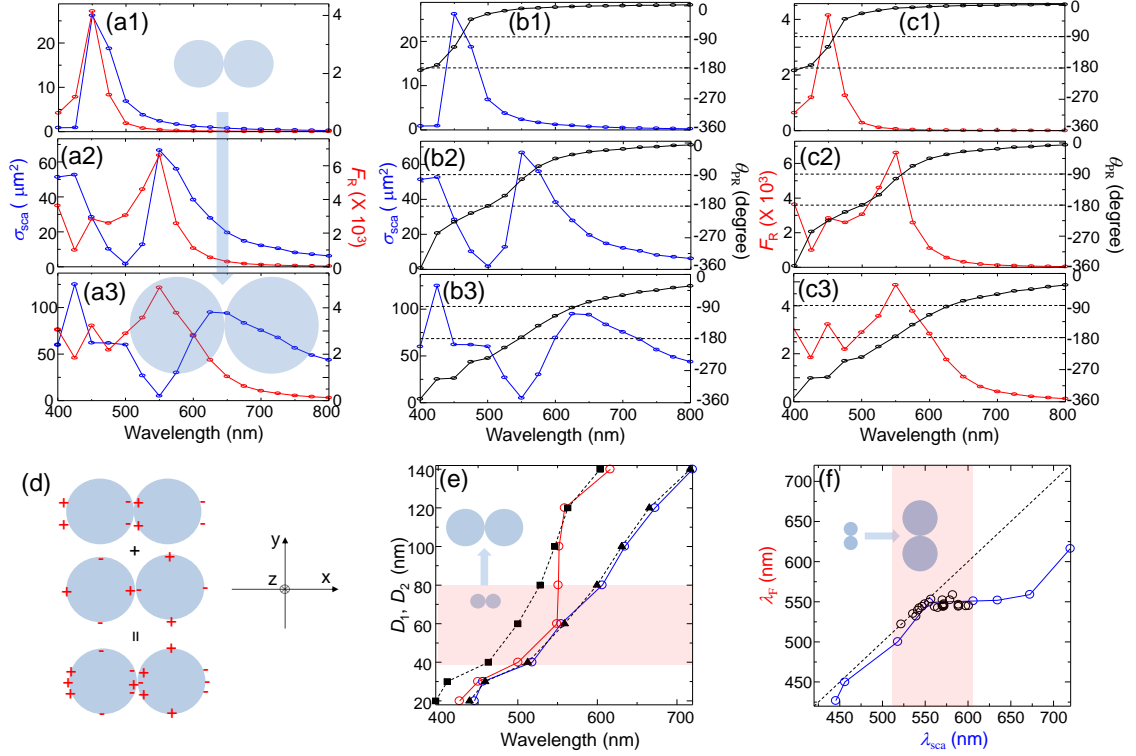


FIG. 10. (a1)–(a3) Diameter dependence of the spectra of σ_{sca} (blue curves) and F_R (red curves) for NW dimers with D_1, D_2 of 30, 60, and 100 nm, respectively. (b1)–(b3) Diameter dependence of the σ_{sca} spectra (blue curves) with θ_{PR} (upper and lower dashed lines indicate -90° and -180° , respectively) of 1D HS of NW dimers with D_1, D_2 of 30, 60, and 100 nm, respectively. (c1)–(c3) Diameter dependence of the F_R spectra (red curves) with θ_{PR} (upper and lower dashed lines indicate -90° and -180° , respectively) of 1D HS of NW dimers with D_1, D_2 of 30, 60, and 100 nm, respectively. (d) Charge distributions

of dipole (upper), quadrupole (middle), and DQ-coupled (lower) resonance for symmetric NW dimer, respectively. The coordinate system is common to that shown in Fig. 9. (e) Diameter dependences of λ_{sca} (blue open circles with line), λ_{F} (red open circles with line), $\theta_{\text{PR}} = 90^\circ$ (black close circles with dashed line, DD resonance), and $\theta_{\text{PR}} = 180^\circ$ (black close triangles with dashed line, DQ resonance) for dimers with D_1, D_2 of 20 nm to 140 nm. The translucent red box indicates $40 \text{ nm} < D_1, D_2 < 80 \text{ nm}$ indicated from Fig. 4(d). (f) Calculated relationship between λ_{sca} and λ_{F} (blue open circles with line) for dimers with D_1, D_2 of 20 nm to 140 nm. Experimental relationship between λ_{sca} and λ_{F} (black open circles) taken from Fig. 8. The translucent red box indicates the range of λ_{sca} expected by Figs. 4(d).

Figures 11(a1)–11(a3) show the spectra of σ_{sca} and F_{R} of the asymmetric NW dimers obtained by changing D_1 from 60 to 140 nm while maintaining $D_2 = 60 \text{ nm}$ with respect to the diameter ratios between the NW dimers in Fig. 4(e). As D_1/D_2 increased, the positions of λ_{sca} and λ_{F} deviated from each other, and both exhibited redshifts while maintaining their spectral deviation constant. Figures 11(b1)–11(b3) show the spectra of σ_{sca} with θ_{PR} . λ_{sca} redshifts with increasing D_1/D_2 and is located at a θ_{PR} of -90° , indicating that the maxima of σ_{sca} corresponds to the DD-coupled plasmon resonance of

the two NWs.^{27,28} Figures 11(c1)–11(c3) show the spectra of F_R with θ_{PR} . The λ_F redshifts with increasing D_1/D_2 and is located at a θ_{PR} of approximately -90° until 60 nm, indicating that F_R is generated by DD-coupled plasmon resonance.^{27,28} However, the λ_F redshifts at a θ_{PR} of -135° . The value of -135° in Figs. 11(c2) and 11(c3) and the constant deviation between λ_{sca} and λ_F in Figs. 11(a2) and 11(a3) indicate that the depolarization of DQ-coupled plasmon cannot be parallel to the incident light polarization. The possible charge distribution of such a situation is illustrated in Fig. 11(d).³⁹ As increasing diameter of the larger NW, its quadrupole resonance redshifts and is overlapped with dipole resonance of the smaller NW. The overlapping results in the DQ-coupled resonance.^{27,28} We consider that the asymmetry in the charge distribution against the x-z plane results in λ_F at a θ_{PR} of -135° not -180° . Figure 11(e) shows D_1/D_2 dependence of λ_{sca} and λ_F with θ_{PR} of -90° , -135° , and -180° . The translucent red box indicates the range $60 \text{ nm} < D_1 < 80 \text{ nm}$ by considering Fig. 4(e). Both λ_{sca} and F_R follow the θ_{PR} of -90° at $D_1 = 60 \text{ nm}$, indicating that the F_R is generated by DD-coupled plasmon resonance. With increasing $D_1 > 60 \text{ nm}$, λ_{sca} keeps following θ_{PR} of -90° , but λ_F moves to a θ_{PR} of -135° , indicating that the DQ-coupled plasmon as in Fig. 11(d) becomes dominant for generating F_R for $D_1 > 60 \text{ nm}$. Figure 11(f) shows the relationship between λ_{sca} and λ_F taking from Fig. 11(e), along with the experimental

relationship taking from Fig. 8. The translucent red box indicates the range of λ_{sca} for $60 \text{ nm} < D_1 < 80 \text{ nm}$. The first trend was reasonably reproduced by the calculation. However, the second trend was not clearly observed in the calculated relationship, indicating that it was mainly caused by the diameter effect in Fig. 10 and not by the asymmetry effect in Fig. 11. This indication is supported by the distribution of the NW diameter, $40 \text{ nm} < D_1 < 90 \text{ nm}$, in Fig. 4(d) and the degree of asymmetry in Fig. 4(e) $0.5 < D_1/D_2 < 2.0$.

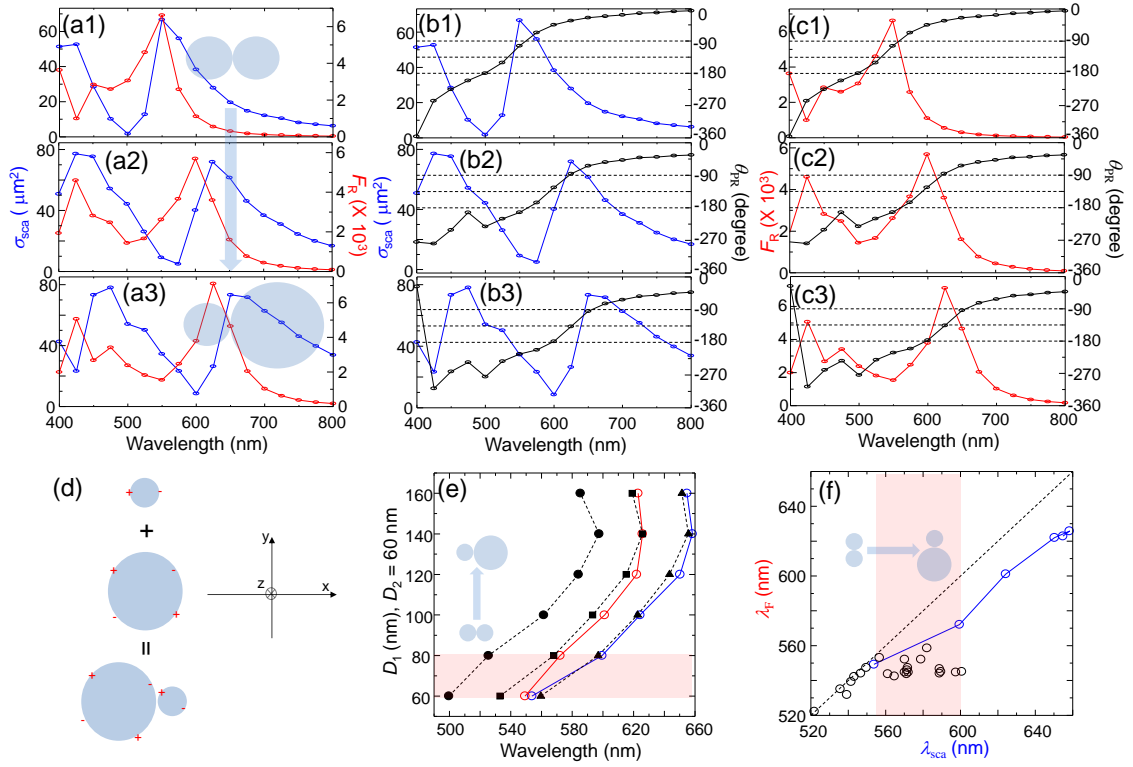


FIG. 11. (a1)–(a3) D_1 dependence of the spectra of σ_{sca} (blue curves) and F_R (red curves) for dimers with D_1 of 60, 100, and 140 nm, respectively, with maintaining $D_2 = 60 \text{ nm}$. (b1)–(b3) D_1 dependence of the σ_{sca} spectra (blue curves) with θ_{PR} (upper, 0 to 360 degrees) for D_1 of 60, 100, and 140 nm, respectively. (c1)–(c3) D_1 dependence of the F_R spectra (red curves) with θ_{PR} (lower, 0 to 360 degrees) for D_1 of 60, 100, and 140 nm, respectively. (d) Schematic diagram of a dimer with two particles of diameter D_1 and D_2 , showing the coordinate system (x, y, z). (e) D_1 dependence of the λ_{PR} (nm) for $D_2 = 60 \text{ nm}$, showing a red shaded region for λ_{sca} between 60 and 80 nm. (f) D_1 dependence of the λ_{PR} (nm) for $D_2 = 60 \text{ nm}$, showing a red shaded region for λ_{sca} between 60 and 80 nm.

middle, and lower dashed lines indicate -90° , -135° and -180° , respectively) of 1D HS of NW dimers with D_1 of 60, 100, and 140 nm, respectively, with $D_2 = 60$ nm. (c1)–(c3) D_1 dependence of the F_R spectra (red curves) with θ_{PR} (upper, middle, and lower dashed lines indicate -90° , -135° and -180° , respectively) of 1D HS of NW dimers with D_1 of 60, 100, and 140 nm, respectively, with $D_2 = 60$ nm. (d) Charge distributions of dipole (upper), quadrupole (middle), and DQ-coupled (lower) resonance for asymmetric NW dimer, respectively. The coordinate system is common to that of Fig. 9. (e) D_1 dependences of λ_{sca} (blue open circles with line), λ_F (red open circles with line), $\theta_{PR} = 90^\circ$ (black close circles with dashed line, DD resonance), $\theta_{PR} = 135^\circ$ (black close squares with dashed line), and $\theta_{PR} = 180^\circ$ (black close triangles with dashed line, DQ resonance) for dimers with D_1 of 60 nm to 140 nm, with maintaining D_2 of 60 nm. The translucent red box indicates the range of $60 \text{ nm} < D_1 < 80 \text{ nm}$ indicated from Fig. 4(e). (f) Calculated relationship between λ_{sca} and λ_F (blue open circles with line) for dimers with D_1 of 60 nm to 140 nm with $D_2 = 60$ nm. Experimental relationship between λ_{sca} and λ_F (black open circles) taken from Fig. 8. The translucent red box indicates the range of λ_{sca} expected by Fig. 4(e).

V. Conclusion

We developed a spectroscopic technique to measure the F_R of 1D HSs along single NW dimers using UFSEF of dye molecules by selecting λ_{ex} suitable for observing whole spectral shapes of the F_R . The F_R spectra were obtained by dividing the spectra of the UFSEF of single NW dimers by a reference UFSEF spectrum, in which the spectral variation in F_R were averaged out. The derived F_R spectra did not frequently match the σ_{sca} spectra. This mismatch indicates that F_R is not generated by superradiant plasmon resonance. These results were examined using FDTD calculations by changing the morphologies of symmetric and asymmetric NW dimers. The mismatch between the F_R and σ_{sca} spectra was reproduced by increasing the diameters of the symmetric NW dimers. The θ_{PR} analysis revealed that the DQ-coupled plasmon resonance, which is subradiant, mainly generates F_R for dimers with NW diameters higher than 80 nm. This spectroscopic method, which directly measures F_R , is applicable to various plasmonic systems coupled with molecular excitons.^{21,22,40} Particularly, this method will be useful for large plasmonic systems in which F_R is dominated by subradiant modes.⁴¹

Acknowledgements

This work was supported by a JSPS KAKENHI Grant-in-Aid for Scientific Research

(C) (grant number 21K04935). The authors thank to Prof. Jeyadevan Balachandran (the University of Shiga Prefecture) for silver nanowires.

LIST OF ABBREVIATIONS

- $\hat{\mathbf{A}}$, Operators of vector potential
- D_1 , diameter of silver NW in Fig. 9(b)
- D_2 , diameter of silver NW in Fig. 9(b)
- DD, dipole–dipole
- DQ, dipole–quadrupole
- $\Delta\omega_R$, radiative decay rates of plasmon resonance
- $\Delta\omega_{NR}$, nonradiative decay rates of plasmon resonance
- E^l , amplitudes of the incident electric field
- E^{loc} , amplitudes of the enhanced local electric fields
- EM, electromagnetic
- F , Purcell factor
- FDTD, finite-difference time-domain
- F_R , electromagnetic enhancement factor in Eq. (1)
- Γ_{r0} , total radiative decay rate of dye molecule in a free space
- Γ_{Rad} , total radiative decay rates of a molecule enhanced by F_R
- Γ_{int} , total internal relaxation rate of molecule
- γ_{r0} , radiative decay rates at λ_{em} of dye molecule in a free space
- HS, hotspot

n , refractive index around the nanostructure
 NA, numerical aperture
 NP, nanoparticle
 NW, nanowire
 λ , wavelength of light
 λ_{em} , wavelength of emission light
 λ_{ex} , wavelength of excitation light
 λ_F , wavelength of maximum of F_R
 λ_{sca} , wavelength of maximum of σ_{sca}
 1D HS, one-dimensional hotspot
 $\hat{\mathbf{p}}$, operators of momentum
 Q , quality factor of plasmon resonance
 R6G, rhodamine 6G
 SEA, surface-enhanced absorption
 SEF, surface-enhanced fluorescence
 SEM, scanning electron microscope
 SE(R)RS, surface-enhanced (resonant) Raman scattering
 σ_{abs} , absorption cross-section
 σ_{ext} , extinction cross-section
 σ_{sca} , Rayleigh scattering cross-section
 σ_{Ufflo} , cross-section of ultrafast fluorescence without EM enhancement
 σ_{UFSEF} , cross-section of UFSEF
 θ_{PR} , phase retardation of E^{loc} against E^I
 UFSEF, ultrafast surface enhanced fluorescence

V_p , mode volume of plasmon

References

- ¹ T. Itoh, Y. S. Yamamoto, and Y. Ozaki, Plasmon-enhanced spectroscopy of absorption and spontaneous emissions explained using cavity quantum optics, *Chem. Soc. Rev.* **46**, 3904 (2017).
- ² H. Xu, E. J. Bjerneld, M. Käll, and L. Börjesson, Spectroscopy of single haemoglobin molecules by surface enhanced Raman scattering, *Phys. Rev. Lett.* **83**, 4357 (1999).
- ³ W. Zhu and K. B. Crozier, Quantum mechanical limit to plasmonic enhancement as observed by surface-enhanced Raman scattering. *Nat. Commun.* **5**, 5228 (2014).
- ⁴ C. Ciraci, R. T. Hill, J. J. Mock, Y. Urzhumov, A. I. Fernandez-Dominguez, S. A. Maier, J. B. Pendry, A. Chilkoti, D. R. Smith, Probing the ultimate limits of plasmonic enhancement, *Science* **337**, 1072–1074 (2012).
- ⁵ S. Nie and S. Emory, Probing single molecules and single nanoparticles by surface-enhanced Raman scattering, *Science* **275**, 1102 (1997).
- ⁶ K. Kneipp, Y. Wang, H. Kneipp, L. Perelman, I. Itzkan, R. R. Dasari, and M. Feld, Single molecule detection using surface-enhanced Raman scattering (SERS), *Phys. Rev. Lett.* **78**, 1667 (1997).

⁷ A. M. Michaels, M. Nirmal, and L. E. Brus, Surface enhanced Raman spectroscopy of individual rhodamine 6G molecules on large Ag nanocrystals, *J. Am. Chem. Soc.* **121**, 9932 (1999).

⁸ E. C. Le Ru, M. Meyer, and P. G. Etchegoin, Proof of single-molecule sensitivity in surface enhanced Raman scattering (SERS) by means of a two-analyte technique, *J. Phys. Chem. B* **110**, 1944 (2006).

⁹ A. B. Zrimsek, A. I. Henry, and R. P. Van Duyne, Single molecule surface-enhanced Raman spectroscopy without nanogaps, *J. Phys. Chem. Lett.* **4**, 3206 (2013).

¹⁰ J. J. Baumberg, J. Aizpurua, M. H. Mikkelsen, and D. R. Smith, Extreme nanophotonics from ultrathin metallic gaps, *Nat. Mater.* **18**, 668 (2019).

¹¹ T. Itoh, Y. S. Yamamoto, H. Tamaru, V. Biju, S. Wakida, and Y. Ozaki, Single-molecular surface-enhanced resonance Raman scattering as a quantitative probe of local electromagnetic field: The case of strong coupling between plasmonic and excitonic resonance, *Phys. Rev. B* **89**, 195436 (2014).

¹² T. Itoh and Y. S. Yamamoto, Reproduction of surface-enhanced resonant Raman scattering, and fluorescence spectra of a strong coupling system composed of a single silver nanoparticle dimer and a few dye molecules, *J. Chem. Phys.* **149**, 244701 (2018).

¹³ T. Itoh, Y. S. Yamamoto, and T. Okamoto, Anti-crossing property of strong coupling

system of silver nanoparticle dimers coated with thin dye molecular films analyzed by electromagnetism, *J. Chem. Phys.* **152**, 054710 (2020).

¹⁴ T. Itoh and Y. S. Yamamoto, Between plasmonics and surface-enhanced resonant Raman spectroscopy: toward single-molecule strong coupling at a hotspot, *Nanoscale* **13**, 1566 (2021).

¹⁵ R. Esteban, J. J. Baumberg, and J. Aizpurua, Molecular optomechanics approach to surface-enhanced Raman scattering, *Acc. Chem. Res.* **55**, 1889–1899 (2022).

¹⁶ R. F. Ribeiro, L. A. Martínez-Martínez, M. Du, J. Campos-Gonzalez-Angulo, and J. Yuen-Zhou, Polariton chemistry: controlling molecular dynamics with optical cavities. *Chem. Sci.* **9**, 6325 (2018).

¹⁷ K. Yoshida, T. Itoh, H. Tamaru, V. Biju, M. Ishikawa, and Y. Ozaki, Quantitative evaluation of electromagnetic enhancement in surface-enhanced resonance Raman scattering from plasmonic properties and morphologies of individual Ag nanostructures, *Phys. Rev. B* **81**, 115406 (2010).

¹⁸ K. J. Savage, M. M. Hawkeye, R. Esteban, A. G. Borisov, J. Aizpurua, and J. J. Baumberg, Revealing the quantum regime in tunnelling plasmonics, *Nature* **491**, 574 (2012).

¹⁹ T. Itoh, M. Iga, H. Tamaru, K. Yoshida, V. Biju, and M. Ishikawa, Quantitative

evaluation of blinking in surface enhanced resonance Raman scattering and fluorescence by electromagnetic mechanism, *J. Chem. Phys.* **136**, 024703 (2012).

²⁰ T. Itoh, Y. S. Yamamoto, V. Biju, H. Tamaru, and S. Wakida, Fluctuating single sp^2 carbon clusters at single hotspots of silver nanoparticle dimers investigated by surface-enhanced resonance Raman scattering, *AIP Adv.* **5**, 127113 (2015).

²¹ S. Y. Ding, E. M. You, Z. Q. Tian, and M. Moskovits, Electromagnetic theories of surface-enhanced Raman spectroscopy, *Chem. Soc. Rev.* **46**, 4042–4076 (2017).

²² T. Itoh, M. Prochazka, Z.-C. Dong, W. Ji, Y. S. Yamamoto, Y. Zhang, and Y. Ozaki, Toward a new era of SERS and TERS at the nanometer scale: from fundamentals to innovative applications, *Chem. Rev.* **123**, 1552 (2023).

²³ T. Itoh, T. Y. S. Yamamoto, Y. Kitahama, and J. Balachandran, One-dimensional plasmonic hotspots located between silver nanowire dimers evaluated by surface-enhanced resonance Raman scattering, *Phys. Rev. B* **95**, 115441 (2017).

²⁴ T. Itoh, T. Y. S. Yamamoto, and J. Balachandran, Propagation mechanism of surface plasmons coupled with surface-enhanced resonant Raman scattering light through a one-dimensional hotspot along a silver nanowire dimer junction, *Phys. Rev. B* **103**, 245425 (2021).

²⁵ J. J. Sakurai, *Advanced Quantum Mechanics* (Addison-Wesley, Reading, MA, 1967);

W. Heitler, *The Quantum Theory of Radiation* (Oxford Univ. Press, MA, 1954).

²⁶ T. Itoh, Y. S. Yamamoto, Demonstration of electromagnetic enhancement correlated to optical absorption of single plasmonic system coupled with molecular excitons using ultrafast surface-enhanced fluorescence, *J. Chem. Phys.* **159**, 2 034709 (2023).

²⁷ T. Itoh and Y. S. Yamamoto, Contribution of subradiant plasmon resonance to electromagnetic enhancement in resonant Raman with fluorescence examined by single silver nanoparticle dimers, *J. Phys. Chem. C* **127**, 5886–5897 (2023)

²⁸ T. Itoh and Y. S. Yamamoto, Correlated polarization dependences between surface-enhanced resonant Raman scattering and plasmon resonance elastic scattering showing spectral uncorrelation to each other, *J. Phys. Chem. B* **127**, 4666–4675 (2023).

²⁹ T. Itoh, Y. S. Yamamoto, and T. Okamoto, Absorption cross-section spectroscopy of a single strong-coupling system between plasmon and molecular exciton resonance using a single silver nanoparticle dimer generating surface-enhanced resonant Raman scattering, *Phys. Rev. B*, **99**, 235409 (2019).

³⁰ C. F. Bohren, and D. R. Huffman, *Absorption and Scattering of Light by Small Particles* (Wiley, New York, 1983).

³¹ E. C. Le Ru, P. G. Etchegoin, J. Grand, N. Féridj, J. Aubard, and G. Lévi, Mechanisms of spectral profile modification in surface-enhanced fluorescence, *J. Phys. Chem. C* **111**,

44, 16076–16079 (2007).

³² T. Itoh, Y. S. Yamamoto, H. Tamaru, V. Biju, N. Murase, and Y. Ozaki, Excitation laser energy dependence of surface-enhanced fluorescence showing plasmon-induced ultrafast electronic dynamics in dye molecules, *Phys. Rev. B* **87**, 235408 (2013).

³³ B. Li, S. Ye, I. E. Stewart, S. Alvarez, and B. J. Wiley, Synthesis and Purification of Silver Nanowires To Make Conducting Films with a Transmittance of 99%, *Nano Lett.* **15**, 6722 (2015).

³⁴ P. Lee and D. Meisel, Adsorption and surface-enhanced Raman of dyes on silver and gold sols, *J. Phys. Chem.* **86**, 3391 (1982).

³⁵ P. B. Johnson, and R. W. Christy, Optical constants of the noble metals, *Phys. Rev. B* **6**, 4370–4379 (1972).

³⁶ P. Johansson, H. Xu, and M. Käll, Surface-enhanced Raman scattering and fluorescence near metal nanoparticles, *Phys. Rev. B* **72**, 035427 (2005).

³⁷ C. M. Galloway, P. G. Etchegoin, and E. C. Le Ru, *Phys. Rev. Lett.* **103**, 063003 (2009).

³⁸ Y. Tanaka, A. Sanada, K. Sasaki, Nanoscale interference patterns of gap-mode multipolar plasmonic fields, *Sci. Rep.* **2**, 764 (2012).

³⁹ L. V. Brown, H. Sobhani, J. B. Lassiter, P. Nordlander, N. J. Halas, Heterodimers:

plasmonic properties of mismatched nanoparticle pairs, *ACS Nano* **4**, 819–832 (2010).

⁴⁰J. Langer et al., Present and future of surface-enhanced Raman scattering, *ACS Nano* **14**, 28–117 (2020).

⁴¹S. Zhang, K. Bao, N. J. Halas, H. Xu, and P. Nordlander, Substrate-Induced Fano resonances of a plasmonic nanocube: a route to increased-sensitivity localized surface plasmon resonance sensors revealed, *Nano Lett.* **11**, 1657–1663 (2011); M. Pellarin, J. Ramade, J. M. Rye, C. Bonnet, M. Broyer, M.-A. Lebeault, J. Lermé, S. Marguet, J. R.G. Navarro, and E. Cottancin, Fano transparency in rounded nanocube dimers induced by gap plasmon coupling, *ACS Nano* **10**, 11266–11279 (2016).